

Chapter 2

Methods

The history of scientific enquiry from the earliest times to the present day might be neatly summarized into three questions: what is the nature of light itself, of matter itself, and of the interaction agent?

John Weiner and Frederico Nunes [1]

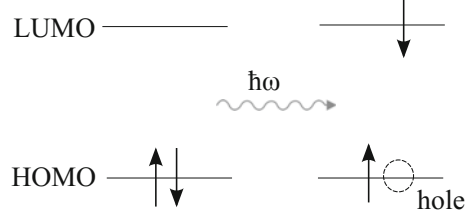
The aim of this chapter is to build a toolbox of methods which can give insight into the functional mechanisms of both organic and biological systems. I will begin by reviewing some key ideas from solid state physics and the theory of open quantum systems. These approaches have a long history in the literature and provide a solid basis on which to build new methods for organic and biological systems. I will then introduce the recently developed experimental technique of 2D electronic spectroscopy, which can provide crucial information concerning ultrafast quantum and vibrational dynamics. Nonetheless, 2D spectroscopy results are difficult to interpret and I will discuss approaches to untangling the complex information contained in 2D spectra.

2.1 Excitonic Models

If a molecule absorbs a quantum of energy corresponding to a transition between two molecular orbitals, an electron can be transferred from the highest occupied molecular orbital (the HOMO) to the lowest unoccupied molecular orbital (the LUMO). This process leaves a hole in the HOMO and is illustrated in Fig. 2.1. The resulting bound electron-hole pair is known as an ‘exciton’ [2].

In a molecular dimer, interactions between the molecules cause the exciton to delocalise across both molecules. Note that the interactions between molecules which lead to excitons are often electrostatic [3]. In order to write down the interaction between two molecules, we consider their charge distributions, $\rho_1(\vec{r})$ and $\rho_2(\vec{r})$ and define the charge of molecule i as:

Fig. 2.1 Sketch of HOMO-LUMO transition: when energy is absorbed, an electron is transferred from the HOMO to the LUMO



$$q_i = \int d\vec{r} \rho_i(\vec{r}) \quad (2.1)$$

and its dipole moment as:

$$\vec{\mu}_i = \int d\vec{r} \rho_i(\vec{r})(\vec{r} - \vec{r}_i) \quad (2.2)$$

(the concept of dipole moment will be discussed in detail in Sect. 2.3.2).

Then the Coulomb interaction can be expanded in the multipole expansion [3]:

$$J_{12} = \frac{1}{4\pi\epsilon} \left[\frac{q_1 q_2}{R} + \frac{q_1(\vec{\mu}_2 \cdot \hat{R}) - q_2(\vec{\mu}_1 \cdot \hat{R})}{R^2} + \frac{\vec{\mu}_1 \cdot \vec{\mu}_2 - 3(\vec{\mu}_1 \cdot \hat{R})(\vec{\mu}_2 \cdot \hat{R})}{R^3} + \dots \right] \quad (2.3)$$

Here, $\vec{R} = \vec{r}_2 - \vec{r}_1$ where $\vec{r}_{1,2}$ is the position vector of molecule 1 or 2 and ϵ is the permittivity. In order for this expansion to be valid, the distance between molecules, R , must be larger than the charge distributions of individual molecules. Note that if the molecules are uncharged the third order term (the dipole-dipole interaction) dominates over the first and second order terms.

These molecular interactions mix the original states to form new states, which are superpositions of the original states. Formally, if the two molecules are identical and the excitation is initially on molecule 1: $\phi_1^* \phi_2$, or on molecule 2: $\phi_1 \phi_2^*$, the new states become the superpositions $1/\sqrt{2}(\phi_1^* \phi_2 \pm \phi_1 \phi_2^*)$, as shown in Fig. 2.2a [2]. In general, the degree of delocalisation of the excitons depends on the original site energies and couplings. Crucially, the mixing alters the energy spectrum of the system. In particular, the energies of the two new states become split (by an energy difference equal to twice the interaction between the molecules if they are identical). This effect is known as ‘Davydov splitting’ [4]. In order to calculate the effects of the new energy spectrum on the material’s photophysics, the transition dipole moments of the new states can be written in terms of the original transition dipole moments [5]:

$$\vec{\mu}_{\alpha 0} = \sum_i V_{\alpha i}^{-1} \vec{\mu}_{i0} \quad (2.4)$$

Here, $\vec{\mu}_{i0}$ is the transition dipole moment of the original site i from the ground state (0), whilst $\vec{\mu}_{\alpha 0}$ is the transition dipole moment of the eigenstate α from the ground

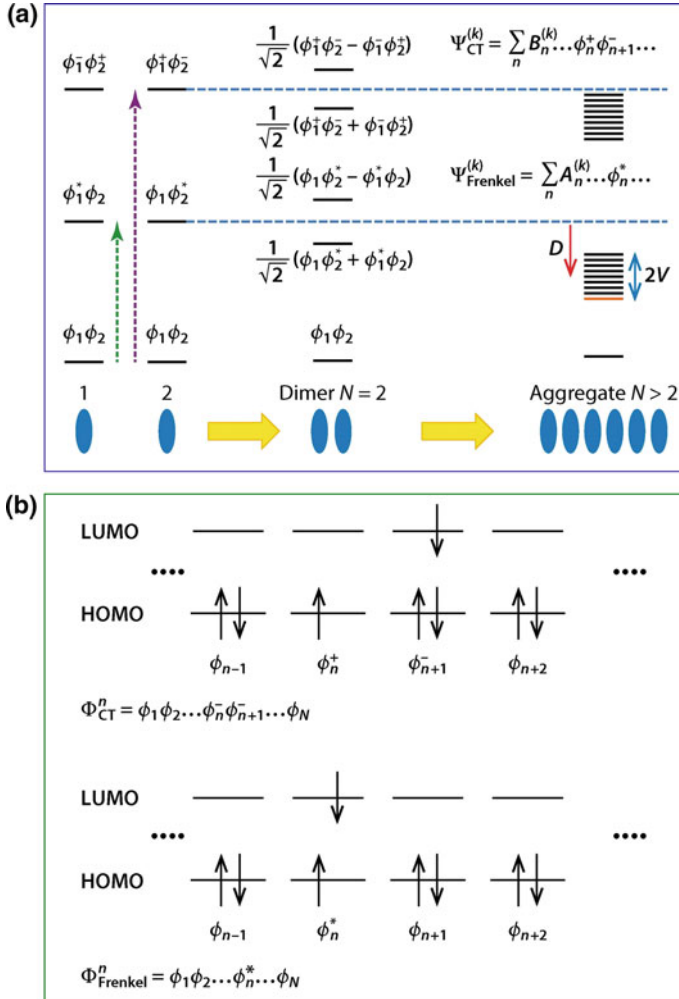


Fig. 2.2 Sketches of the energy spectrum and HOMO and LUMO bands in Frenkel and charge transfer excitons. **a** As isolated molecules are brought closer to each other to form a dimer, they begin to interact and their energy levels split. In an aggregate, a band of states forms. **b** The HOMO and LUMO in a Frenkel exciton (*lower panel*), showing the electron and hole on the same molecule. In a charge transfer exciton (*upper panel*), the electron and hole are on adjacent molecules. Figure adapted from [2]

state. V is the operator which diagonalises the site Hamiltonian (which is defined by the individual molecules' energies and couplings) in order to obtain the excitonic Hamiltonian:

$$H_{\text{exciton}} \equiv V^{-1} H_{\text{site}} V \quad (2.5)$$

In a molecular aggregate the exciton becomes delocalised across multiple molecules, leading to a band of exciton states. This was first shown by Frenkel in the 1930s [6, 7] and this type of exciton is therefore known as a Frenkel exciton. Crucially, the electron and hole remain localised on the same molecule, as shown in Fig. 2.2b (lower panel). This type of exciton is often observed in organic and biological molecules and we will use it extensively in the following chapters. Note that excitons can also be classified as either singlet or triplet excitons, depending on the spin state of the electrons involved [2]. For example, if the electrons in the lower and upper states have opposite spins, as in the bottom panel of Fig. 2.2b and precess out of phase with each other, they are in an overall spin singlet state, $S = 0$. If they precess in phase or have the same spin orientations, the spin state is triplet, $S = 1$. Triplet excitons are stabilised with respect to singlets by the exchange energy (due to reduced electron-electron repulsions). However they are optically dark and the singlet to triplet transition is normally a slow process in molecules without heavy atoms because it requires spin-orbit coupling.

Whilst in Frenkel excitons the electron and hole are always localised on the same molecule, in other types of exciton they may lie further apart. For example, in charge transfer (CT) excitons the electron and the hole are localised on adjacent molecules, as shown in Fig. 2.2b (upper panel). Similar to Frenkel states, in molecular dimers and aggregates molecular interactions cause charge transfer states to mix and form new superposition states. Note that Frenkel and CT states can also mix (and this is the origin of the singlet-multiexciton state coupling in pentacene which will be discussed in Chap. 3).

For completeness, in Wannier-Mott excitons the electron and hole are separated by much larger distances (typically ≈ 100 Å) and are only loosely bound [8, 9]. This concept is useful in inorganic semiconductors, where large dielectric constants mean that electric field screening reduces the interaction between the hole and the electron. However, organic materials have much smaller dielectric constants, hence here we will only be concerned with Frenkel and charge-transfer excitons [2].

2.2 Energy Transfer and Dissipation

No physical system is completely isolated from its surroundings. In organic and biological systems there are normally a large number of vibrations including solvent modes, intramolecular vibrations, phonons and electromagnetic modes, which all contribute towards the environment. Over time, interactions between the system and its environment lead to decoherence.

In order to treat energy transfer in organic and biological systems, we need to take account of the environment. There are different approaches to doing this, which are valid in different regimes. Förster resonance energy transfer (FRET) is often used in the localised limit, where the coupling between molecules is weak and can be treated as a perturbation. Here, energy transfer occurs between molecules when there is a resonance between the energy gaps of the donor and acceptor states. The

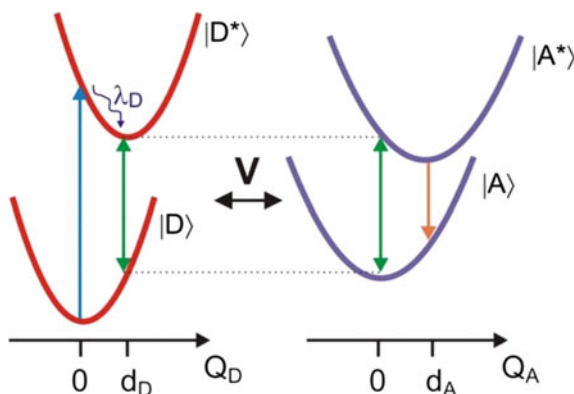


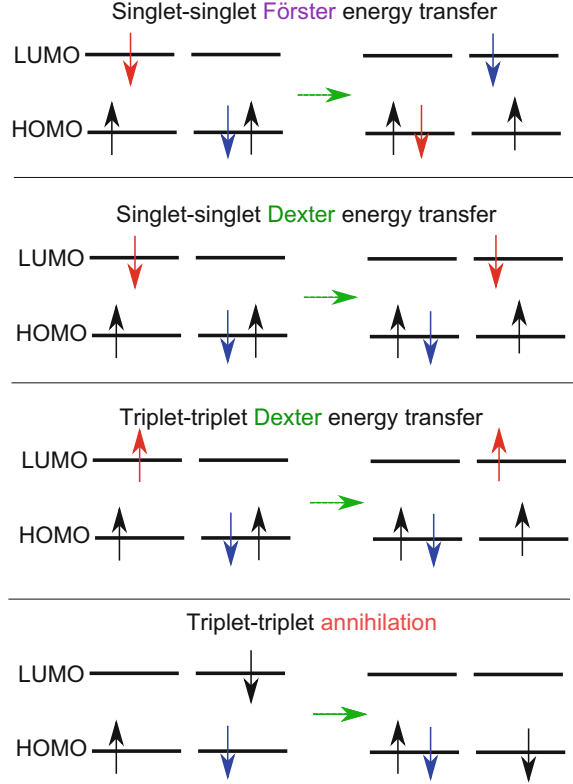
Fig. 2.3 Förster resonance energy transfer: The donor absorbs light, leading to an excited state, $|D^*\rangle$. The donor then relaxes, dissipating its reorganisation energy, λ_D . This creates a resonance between the energy gaps of the donor and acceptor, shown in green. Energy transfer to the acceptor (due to a dipole-dipole interaction) is then followed by further relaxation. Figure taken from [11]

energy transfer process is illustrated in Fig. 2.3 and scales as r^{-6} , where r is the intermolecular distance [10].

An excited donor may also transfer energy to an acceptor state via electron exchange, in a process known as Dexter energy transfer [12]. Unlike in FRET, in Dexter energy transfer the reaction rate decays exponentially with the distance between the donor and acceptor, hence this process is only important at short distances (normally within 10 \AA) [13]. Dexter energy transfer is illustrated in Fig. 2.4, alongside FRET for comparison. As shown in the figure, both singlet-singlet and triplet-triplet Dexter energy transfer are possible and this type of interaction can also lead to triplet-triplet annihilation. In the latter case, two triplet excitations recombine to form a singlet excitation in a manner which is essentially the reverse of the singlet fission process which will be discussed in Chap. 3.

However, when molecules are close together, coupling between them may be strong and Förster theory is no longer valid. For example, this is true for the pigment protein complexes which carry out photosynthesis and will be discussed in detail in Chap. 4. Collective excitations between pigments are known as excitons, as discussed in the previous section, and an exciton coupling theory is required. Below, we describe how energy dissipation is taken into account in this case using one such theory, known as Bloch-Redfield theory. In Bloch-Redfield theory, instead of assuming that the coupling between molecules is weak, we assume that the coupling between the system and the environment is weak.

Fig. 2.4 Excitations in Dexter and Förster resonance energy transfer. Figure adapted from figures by Che-Wei Chang, taken from [14]



2.2.1 Description of the Bath

In order to treat dissipation, we first need to define our system and its environment. Here we consider the general case, where H is the Hamiltonian of a system with a number of states, indexed by i . Couplings, J , exist between the states (which might arise from electrostatic interactions, for example). The Hamiltonian can therefore be written as:

$$H = \sum_i \varepsilon_i |i\rangle \langle i| + \sum_{i \neq j} J_{ij} |i\rangle \langle j| \quad (2.6)$$

where ε_i is the energy of state i . We place this system in a bath of k harmonic oscillators, with frequencies ω_k , described by the bosonic annihilation and creation operators b_k and b_k^\dagger . The bath Hamiltonian takes the form:

$$H_B = \sum_k \omega_k b_k^\dagger b_k \quad (2.7)$$

where we have set the reduced Planck constant $\hbar = 1$. The sites interact with the bath, leading to decoherence over time. We assume that the interaction of the sites with the bath is linear, as follows:

$$H_{IB} = \sum_{i,k} g_{ik} |i\rangle \langle i| (b_{ik} + b_{ik}^\dagger) \quad (2.8)$$

Here g_{ik} are constants describing the coupling between the sites and the bath modes. These couplings are often difficult to determine experimentally and an alternative approach is to use the spectral function, defined by [15]:

$$J_s(\omega) = \sum_k g_k^2 \delta(\omega - \omega_k) \quad (2.9)$$

The form of the spectral function can be chosen depending on the problem at hand. One possible choice for irreversible relaxation is the over-damped Brownian oscillator spectral function, given by [16]:

$$J_s(\omega) = 2\lambda \frac{\omega\gamma}{\omega^2 + \gamma^2} \quad (2.10)$$

(here we assume that all sites have the same coupling to the bath). γ sets the dynamical response time of the bath. The reorganization energy of the bath, λ , is a measure of the strength of the coupling of the sites to the bath. This defines g in Eq. 2.8.

Overall, the total Hamiltonian for the system, the bath and the coupling between the system and the bath is given by:

$$H_{\text{total}} = H + H_B + H_{IB} \quad (2.11)$$

2.2.2 Bloch-Redfield Theory

As discussed above, Bloch-Redfield theory can be used to model the dissipation of energy over time. Here I present an overview of Bloch-Redfield theory, which follows that given in Blum [17]. I use the reduced density matrix and the interaction picture, which are described in more detail in appendices A and B respectively.

I start by writing the time evolution of the reduced density matrix in the interaction picture with respect to H_{total} (see Appendix B):

$$\dot{\rho}(t)_{SI} = -(i/\hbar) \text{Tr}_B[V(t)_I, \rho(0)_I] - (1/\hbar)^2 \int_0^t dt' \text{Tr}_B[V(t)_I, [V(t')_I, \rho(t')_I]] \quad (2.12)$$

where Tr_B represents taking the trace over the bath degrees of freedom, ρ_I is the density matrix in the interaction picture and ρ_{SI} is the reduced density matrix in

the interaction picture. $V(t)_I$ is the interaction term in the interaction picture, which describes the interaction between the system and the bath. Note that $V(t)$ is given by H_{IB} in Eq. 2.11, which was defined in Eq. 2.8.

Bloch-Redfield theory makes two main approximations, which introduce irreversibility into the system, allowing energy to be dissipated. The first approximation is that while the bath changes the state of the system over time, the bath itself remains unchanged, hence the density matrix can be written as:

$$\rho(t)_I = \rho(t)_{SI} \rho(0)_B \quad (2.13)$$

where $\rho(0)_B$ represents the state of the bath, which is unchanged over time and is given by a Boltzmann distribution:

$$\rho(0)_B = \exp(-\beta H_B) / Z \quad (2.14)$$

Here Z is the partition function and $\beta = 1/(k_B T)$, where T is temperature. The second approximation is the Markov approximation, which states that the system has no memory of its past, i.e. $\dot{\rho}(t)_{SI}$ only depends on $\rho(t)$ and not on ρ at earlier times. Therefore in Eq. 2.12 we replace $\rho(t')_{SI}$ with $\rho(t)_{SI}$. Under these two approximations, we obtain:

$$\dot{\rho}(t)_{SI} = -(i/\hbar) \text{Tr}_B[V(t)_I, \rho(0)_S \rho(0)_B] - (1/\hbar)^2 \int_0^t dt' \text{Tr}_B[V(t)_I, [V(t')_I, \rho(t)_{SI} \rho(0)_B]] \quad (2.15)$$

We now split the interaction operator into operators which act on the system only, Q_i , and on the bath only, F_i :

$$V(t)_I = \sum_i F(t)_i Q(t)_i \quad (2.16)$$

with:

$$F(t)_i = \exp(i H_B t / \hbar) F_i \exp(-i H_B t / \hbar) \quad (2.17)$$

and

$$Q(t)_i = \exp(i H t / \hbar) Q_i \exp(-i H t / \hbar) \quad (2.18)$$

From comparison to Eq. 2.8, in our case:

$$Q_i = |i\rangle \langle i| \quad (2.19)$$

and

$$F_i = \sum_k g_{ik} (b_k + b_k^\dagger). \quad (2.20)$$

Using these expressions and the substitution $t'' = t - t'$, we can rewrite Eq. 2.15 as:

$$\dot{\rho}(t)_{SI} = -(1/\hbar)^2 \sum_{ij} \int_0^\infty dt'' [Q(t)_i, Q(t-t'')_j \rho(t)_{SI}] \langle F(t'')_i F_j \rangle - [Q(t)_i, \rho(t)_{SI} Q(t-t'')_j] \langle F_j F(t'')_i \rangle \quad (2.21)$$

Here, $\langle F(t'')_i F_j \rangle$ and $\langle F_j F(t'')_i \rangle$ are time correlation functions, which quantify the correlation between the state of the bath at different times. They can be expressed using the density matrix as:

$$\langle F(t)_i F(t')_j \rangle = \text{Tr}_B(F(t)_i F(t')_j \rho(0)_B) \quad (2.22)$$

A final approximation, known as the secular approximation, can also be made. In this approximation, we average over terms which vary rapidly (compared to the relaxation time of the system). This approximation is popular because it guarantees that the diagonal elements of the density matrix are non-negative, which is not always the case for the density matrix obtained directly from the equations above [17]. It also enables more efficient numerical calculations, since the populations and coherences are no longer coupled. However, this loss of some of the interactions between the system and its environment is not always valid and can lead to inaccurate results [18–20].

If we apply the secular approximation, we obtain:

$$\langle m' | \dot{\rho}(t)_{SI} | m \rangle = \delta_{m'm} \sum_{n \neq m} \langle n | \rho(t)_{SI} | n \rangle W_{mn} - \gamma_{m'm} \langle m' | \rho(t)_{SI} | m \rangle \quad (2.23)$$

This is the Master equation, which is an equation of motion for the reduced density matrix, describing the irreversible behaviour of the system. Here, m are eigenstates of the system's Hamiltonian, H , (given by Eq. 2.6) and we have introduced the quantities:

$$W_{mn} = \Gamma_{nmmn}^+ + \Gamma_{nmmn}^- \quad (2.24)$$

$$\gamma_{m'm} = \sum_k (\Gamma_{m'kkm'}^+ + \Gamma_{m'kkm'}^-) - \Gamma_{mmmm'}^+ - \Gamma_{mmmm'}^- \quad (2.25)$$

$$\Gamma_{mkl n}^+ = (1/\hbar)^2 \sum_{ij} \langle m | Q_i | k \rangle \langle l | Q_j | n \rangle \int_0^\infty dt'' \exp(-i\omega_{ln}t'') \langle F(t'')_i F_j \rangle \quad (2.26)$$

$$\Gamma_{mkl n}^- = (1/\hbar)^2 \sum_{ij} \langle m | Q_j | k \rangle \langle l | Q_i | n \rangle \int_0^\infty dt'' \exp(-i\omega_{mk}t'') \langle F_j F(t'')_i \rangle \quad (2.27)$$

and

$$\omega_{mn} = (E_m - E_n)/\hbar \quad (2.28)$$

In order to understand the implications of the Master equation (Eq. 2.23), it is helpful to consider the rate of change of the diagonal and off-diagonal elements of the density matrix separately. From Eq. 2.23, the diagonal elements obey the equation:

$$\dot{\rho}(t)_{mm} = \sum_{n \neq m} \rho(t)_{nn} W_{mn} - \rho(t)_{mm} \sum_{n \neq m} W_{nm} \quad (2.29)$$

The diagonal elements, $\rho_{mm}(t)$, give the probability of state m being occupied as a function of time. This probability increases due to transitions from all other states (labelled as states n) to state m . The rate of change of $\rho_{mm}(t)$ due to these transitions is given by the population in each state n multiplied by the transition rate from state n to state m . Hence W_{mn} in Eq. 2.29 is interpreted as the transition rate from n to m . Similarly, $\rho_{mm}(t)$ decreases due to transitions from state m to other states and this leads to the second (negative) term in Eq. 2.29. The relaxation time of state m , T_1 , is given by the inverse of the sum of the transition rates from m to all other states [11]:

$$T_{1m} = \frac{1}{\sum_{n \neq m} W_{nm}} \quad (2.30)$$

The rates W_{mn} are given by Eq. 2.24 in terms of the rates Γ_{nnmm}^+ and Γ_{nnmm}^- , which include information about the bath obtained from the time correlation functions of the bath operators, $\langle F(t'')_i F_j \rangle$ and $\langle F_j F(t'')_i \rangle$. F_i depends on g_k , according to Eq. 2.20, and g_k determines the spectral density function, $J_s(\omega)$, as seen from Eq. 2.9. Hence we can also write the rates W_{mn} in terms of the spectral density function, $J_s(\omega)$. Putting everything together, we obtain:

$$W_{mn} = \begin{cases} 2\pi |V_{mn}|^2 J(E_m - E_n) [n(E_m - E_n) + 1] & \text{for } E_m > E_n \\ 2\pi |V_{mn}|^2 J(E_n - E_m) n(E_n - E_m) & \text{for } E_m < E_n \end{cases}$$

where $|V_{mn}|^2 = \sum_i |\langle e_m | i \rangle \langle i | e_n \rangle|^2$. Meanwhile, the factor $n(\omega) = (e^{\omega/k_B T} - 1)^{-1}$ ensures that if $E_n > E_m$, the transition rate from n to m is greater than the rate from m to n so that at equilibrium the population probabilities are given by a Boltzmann distribution.

It is also instructive to consider the off-diagonal density matrix elements, $\rho_{mn}(t)$. From Eq. 2.23, we have:

$$\langle m | \dot{\rho}(t)_{SI} | n \rangle = \left[\Gamma_{nnmm}^+ + \Gamma_{nnmm}^- - \Gamma_{mmmm}^+ - \Gamma_{nnnn}^- - \sum_{k \neq m} \Gamma_{mkkm}^+ - \sum_{k \neq n} \Gamma_{nkkn}^- \right] \langle m | \rho(t)_{SI} | n \rangle \quad (2.31)$$

If we take the real part of the last two terms in Eq. 2.31, the expression we obtain looks very similar to the equation obeyed by the diagonal population elements, Eq. 2.29 [11]:

$$\begin{aligned}
\text{Re} \left(\sum_{k \neq m} \Gamma_{mkkm}^+ + \sum_{k \neq n} \Gamma_{nkkn}^- \right) &= \frac{1}{2} \sum_{k \neq m} W_{km} + \frac{1}{2} \sum_{k \neq n} W_{kn} \\
&= \frac{1}{2} \left(\frac{1}{T_{1m}} + \frac{1}{T_{1n}} \right)
\end{aligned} \tag{2.32}$$

The only difference from Eq. 2.29 is the factor of $\frac{1}{2}$, which means that the off-diagonal coherences decay at half the rate of the population decay. Meanwhile, the real part of the first four terms in Eq. 2.31 can be written as:

$$\begin{aligned}
\text{Re} (\Gamma_{mmnn}^+ + \Gamma_{mmnn}^- - \Gamma_{mmmm}^+ - \Gamma_{nnnn}^-) &= \int_0^\infty dt'' \langle [V_{nn}(t'') - V_{mm}(t'')] [V_{nn}(0) - V_{mm}(0)] \rangle_B \\
&= \int_0^\infty dt'' \langle \Delta V(t'') \Delta V(0) \rangle_B \\
&= \frac{1}{T_2^*}
\end{aligned} \tag{2.33}$$

This term involves a correlation function which accounts for fluctuations in the energy gap between the states m and n. These fluctuations are caused by the energy gap interacting with the bath in a phenomenon known as ‘pure dephasing’. The timescale for pure dephasing is conventionally called T_2^* .

Overall, the dephasing time for the coherences has two contributions; one from the relaxation of the states involved and one from the pure dephasing. It can be written as:

$$\frac{1}{T_2} = \frac{1}{T_2^*} + \frac{1}{2} \left(\frac{1}{T_{1m}} + \frac{1}{T_{1n}} \right) \tag{2.34}$$

As an illustration, we consider the two level system illustrated in Fig. 2.5, with an energy difference of 500 cm^{-1} and coupling of $J = 100 \text{ cm}^{-1}$ between the two states. The states are coupled to a bath, which is described by an over-damped Brownian oscillator spectral function as given in Eq. 2.10. We set $\gamma_j = 900 \text{ cm}^{-1}$ and $\lambda_j = 35 \text{ cm}^{-1}$ and choose the total population on the highest energy site as the initial condition. In Fig. 2.5, we plot the populations of the two eigenstates, which tend to a Boltzmann distribution at long times (the temperature is set to 300K). We also plot the evolution of the site populations, which oscillate due to the non-zero coherences between the two states. Also notice that the populations decay at twice the rate at which the coherences decay, as expected.

The Bloch-Redfield theory described in this section has been used extensively to model energy transfer in photosynthetic pigment protein complexes [21–23] and in Chap. 3 we will also take this approach to model dissipation in thin films of the organic molecule pentacene. Both of these systems exhibit strong interactions between molecules, hence these problems are well suited to the excitonic framework of Redfield theory (as opposed to Förster theory). Note that in Redfield theory we

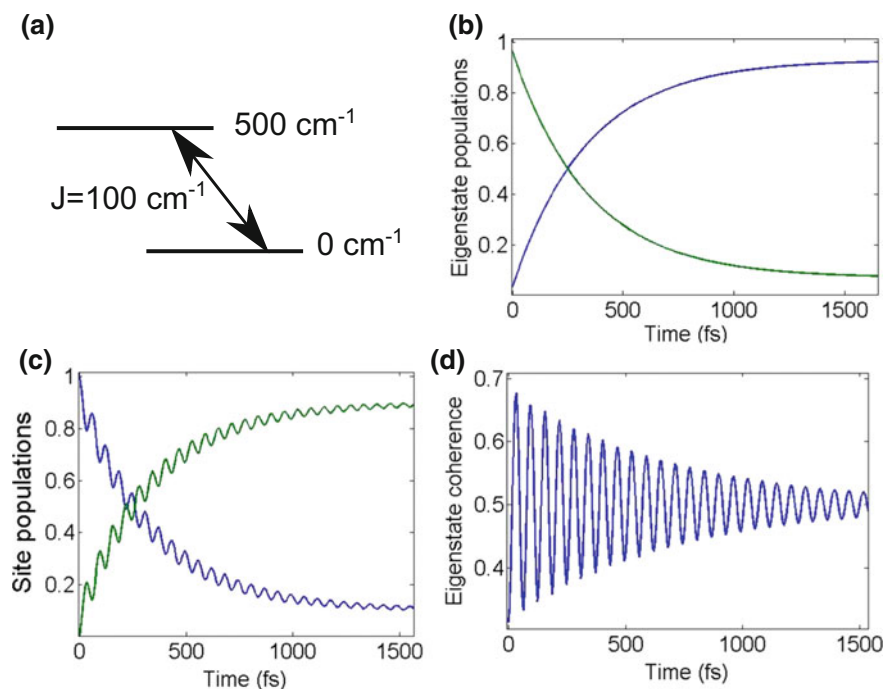


Fig. 2.5 Dynamics for a two level system with Bloch-Redfield dissipation. **a** Two level system. **b** Eigenstate populations as a function of time. **c** Site populations. **d** Coherence between the two eigenstates

assume that the coupling between the system and the bath is weak, which may not always be valid in these systems. One approach to circumventing this problem is to include certain strong vibrational modes in the system itself.

2.3 2D Electronic Spectroscopy

2D Fourier transform spectroscopy was originally applied to nuclear magnetic resonance (NMR) research, where it has proved invaluable in obtaining high resolution structures of complicated molecules. Following this success, 2D spectroscopy was extended to the optical regime in the late 1990s [24] and named 2D electronic or optical spectroscopy. 2D electronic spectroscopy (2DES) employs ultrafast laser pulses and is therefore able to interrogate biological and organic systems at the femtosecond and picosecond timescales on which many molecular processes occur. In conventional 1D spectroscopy the underlying structural and dynamical information is all projected onto a single time or frequency axis, giving congested spectra. By using

2DES, this information can be separated, allowing much greater insight into the system's electronic and vibrational degrees of freedom.

Here, I outline 2DES; much of this discussion is based on work by Mukamel [25] and Fleming [5] (see also Tokmakoff [11] and Hamm [26]). I begin by describing the experimental setup, before examining the underlying theory. 2DES is an example of third order nonlinear spectroscopy, which is the most popular class of nonlinear spectroscopic techniques and also includes transient absorption, photon echo and transient grating experiments. In all of these methods, the signals are determined by the third order polarisation, which I will show how to obtain using nonlinear response formalism. I then introduce the excitonic picture which describes organic and biological systems and explain how Feynman diagrams can be used to understand 2DES signals within this framework. Finally I briefly discuss some of the challenges involved in distinguishing different signals in 2DES spectra.

2.3.1 Experimental Setup

The 2DES experimental setup is shown in Fig. 2.6. There are three incident laser pulses and a signal pulse, centered at times t_1 , t_2 , t_3 and t_s respectively. The ultra-fast pulses employed often have durations of less than 20 fs, leading to broadband excitation. In between the four pulses there are three time periods: the coherence time τ , the waiting time, T , and the detection time, t_d (see Fig. 2.7). Note that the waiting time is sometimes referred to as the population or evolution time in the literature, whilst the detection time is also called the rephasing time.

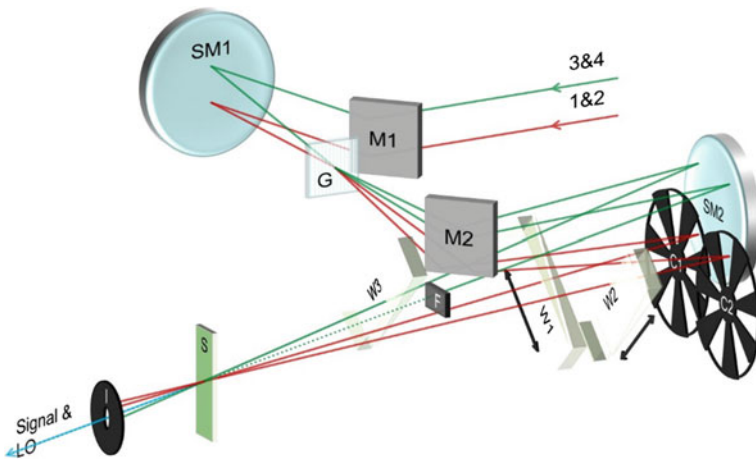
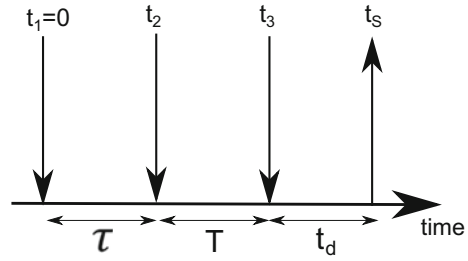


Fig. 2.6 2D spectroscopy experimental setup [27]

Fig. 2.7 Time intervals in third order non-linear spectroscopy



Spectral interference between the signal and a local oscillator pulse is recorded using a spectrometer, which performs a Fourier transform across the detection time. During the experiments, the coherence time is scanned incrementally (often in steps as short as 2 fs). A major challenge in 2DES is maintaining phase stability between pulses 1 and 2 during the coherence time and between pulse 3 and the local oscillator [28]. Full details of the experimental setup can be found in the literature, see for example [24, 28, 29].

2.3.2 Theory Behind 2D Electronic Spectroscopy

Spectroscopy is the study of the interaction between light and matter. Light is an example of an electromagnetic wave, which interacts with matter due to its electric field. When the electric field is incident on a material it becomes polarised, creating an induced dipole moment which depends on the particles' charges (q) and their displacements (\vec{r}):

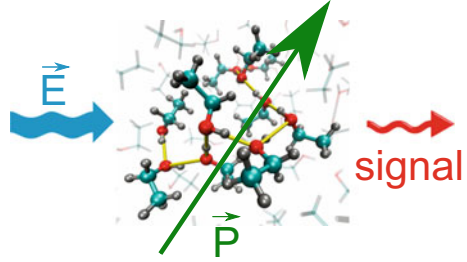
$$\vec{\mu}_{ind} = q\vec{r} \quad (2.35)$$

If the frequency of the optical field is in resonance with a transition between two states of the material then energy can be exchanged between the optical field and the material and light is absorbed or emitted. The electric dipole moment associated with the transition between two states is known as the transition dipole moment. Its direction depends on the polarisation of the transition, whilst its magnitude depends on the material's charge distribution. The transition dipole moment between states ϕ_a and ϕ_b is an intrinsically quantum property of the material and can be written in Dirac notation as:

$$\vec{\mu}_{ab} = \langle \phi_a | \sum_i q_i \vec{r}_i | \phi_b \rangle \quad (2.36)$$

The macroscopic equivalent of the dipole moment is the polarisation, which is defined as a collective dipole moment per unit volume. The polarisation is created by the incident electric fields interacting with the material and it then emits a signal electric field (see Fig. 2.8). With i particles situated at \vec{r}_i , the polarisation is given by

Fig. 2.8 An incident electric field polarises a material, creating a signal. Image of molecules adapted from [30]



[11]:

$$\vec{P}(\vec{r}) = \sum_i \vec{\mu}_i \delta(\vec{r} - \vec{r}_i) \quad (2.37)$$

where δ is the Dirac delta function. The polarisation is related to the electric field, \vec{E} , via the susceptibility, χ [26]. In weak electric fields, this relationship is linear:

$$\vec{P} = \varepsilon_0 \chi \vec{E} \quad (2.38)$$

where ε_0 is the permittivity of free space. However, when there are either several fields (as is the case in 2DES) or very strong fields, the polarisation depends nonlinearly on the electric field. Therefore we expand the polarisation as a power series with respect to \vec{E} :

$$\vec{P} = \varepsilon_0 \left(\chi^{(1)} \vec{E} + \chi^{(2)} \vec{E}^{(2)} + \chi^{(3)} \vec{E}^{(3)} + \dots \right) \quad (2.39)$$

Note that even order susceptibilities vanish in materials with inversion symmetry (including isotropic media), hence the third order term is normally the lowest order nonlinear signal [26]. For n th order nonlinear spectroscopy we require the n th order polarisation, $\vec{P}^{(n)} = \varepsilon_0 \chi^{(n)} \vec{E}^{(n)}$, to calculate the signal. This can be calculated from the n th order density matrix, $\rho^{(n)}(t)$ [25]:

$$\vec{P}^{(n)}(t) = \text{Tr}(\vec{\mu} \rho^{(n)}(t)) \quad (2.40)$$

To calculate $\rho^{(n)}(t)$, we take a semi-classical approach where the material part of the Hamiltonian, H_0 , is treated quantum mechanically, whilst the electromagnetic field, $V(t)$, is treated classically [25]. The total Hamiltonian is:

$$H = H_0 + V(t) \quad (2.41)$$

In the electric dipole approximation, the wavelength of the electromagnetic radiation is assumed to be much larger than the size of the molecules [11]. Then $V(t)$ describes the interaction between the electric field and the transition dipole moment:

$$V(t) = -\vec{E}(t) \cdot \vec{\mu} \quad (2.42)$$

If the external electric field is weak compared to the internal electric fields, we can treat $V(t)$ as a perturbation to the system. It is then convenient to work in the interaction picture, in which the density matrix is given by $\rho(t)_I = U_0^\dagger(t)\rho(t)U_0(t)$ (for further information concerning the interaction picture see appendix B). Here the time evolution operator $U_0(t) = e^{-(i/\hbar)H_0t}$. The density matrix obeys the Liouville equation:

$$i\hbar \frac{\partial \rho(t)_I}{\partial t} = [V(t)_I, \rho(t)_I] \quad (2.43)$$

Following Hamm [26], we take a perturbative expansion in powers of the weak interaction $V(t)$. We then return to the Schrödinger picture and substitute Eq. 2.42 to obtain:

$$\begin{aligned} \rho^{(n)}(t) = & (-i/\hbar)^n \int_{-\infty}^t d\tau_n \int_{-\infty}^{\tau_n} d\tau_{n-1} \dots \int_{-\infty}^{\tau_2} d\tau_1 \vec{E}(\tau_n) \vec{E}(\tau_{n-1}) \dots \vec{E}(\tau_1) \\ & U_0(t) [\vec{\mu}_I(\tau_n), [\vec{\mu}_I(\tau_{n-1}), \dots [\vec{\mu}_I(\tau_1), \\ & \rho(-\infty)] \dots]] U_0^\dagger(t) \end{aligned} \quad (2.44)$$

Here the dipole operator in the interaction picture $\vec{\mu}_I(t) = U_0^\dagger(t)\vec{\mu}U_0(t)$. $\rho(-\infty)$ is the equilibrium density matrix and hence does not evolve over time. We have considered a series of time points τ_n at which the system interacts with a perturbation. Since 2DES is an example of third order nonlinear spectroscopy, we need to calculate the third order polarisation. To do this, again following Hamm [26], we substitute Eq. 2.44 into Eq. 2.40 and change the time variables to those discussed in Sect. 2.3.1 to obtain:

$$\begin{aligned} \bar{P}^{(3)}(t) = & (-i/\hbar)^3 \int_0^\infty dt_d \int_0^\infty dT \int_0^\infty d\tau \vec{E}(t - t_d) \vec{E}(t - t_d - \tau) \vec{E}(t - t_d - T - \tau) \\ & \text{Tr} (\vec{\mu}(t_d + T + \tau) [\vec{\mu}(T + \tau), [\vec{\mu}(\tau), [\vec{\mu}(0), \rho(-\infty)]]]) \end{aligned} \quad (2.45)$$

Equation 2.45 shows that the polarisation is created by the incident electric fields interacting with the material. In the semi-impulsive limit, we assume that the laser pulses are long with respect to the oscillation period of light, but short compared to the timescales of the system [26]. We can therefore write the electric fields as:

$$\vec{E}_1(t) = \vec{E}_{1,0} \delta(t) \exp(\pm i\omega_1 t \mp \vec{k}_1 \cdot \vec{r}) \quad (2.46)$$

$$\vec{E}_2(t) = \vec{E}_{2,0} \delta(t - \tau) \exp(\pm i\omega_2 t \mp \vec{k}_2 \cdot \vec{r}) \quad (2.47)$$

$$\vec{E}_3(t) = \vec{E}_{3,0} \delta(t - \tau - T) \exp(\pm i\omega_3 t \mp \vec{k}_3 \cdot \vec{r}) \quad (2.48)$$

where $\omega_{1,2,3}$ is the frequency of pulse 1, 2 or 3 and $\vec{k}_{1,2,3}$ is the wavevector of pulse 1, 2 or 3. Normally all pulses have the same frequencies, although different frequencies are possible. The wavevectors (and the direction in which the signal is detected)

can be chosen experimentally. Note that in practice the laser pulses are finite, which means that the electric fields can overlap at short waiting times, T . This leads to additional signals and produces the ‘coherent artefact’, which is often observed in 2D spectra at early T [26].

In the limit of infinitely short pulses, the third order response (the signal) is equal to the third order polarisation:

$$S(\tau, T, t_d) = P^{(3)}(t) \quad (2.49)$$

The polarisation acts as a source, generating electric fields in the directions $\vec{k}_s = \pm\vec{k}_1 \pm \vec{k}_2 \pm \vec{k}_3$. In 2DES, normally the rephasing (R) and non-rephasing (NR) signals are measured at $\vec{k}_{I/II} = \mp\vec{k}_1 \pm \vec{k}_2 + \vec{k}_3$. Conventional 2D spectra are obtained by taking Fourier transforms of the signal along both t_d and τ , to obtain $S_{R/NR}(\omega_\tau, T, \omega_{t_d})$:

$$S_{R/NR}(\omega_\tau, T, \omega_{t_d}) = \int_0^\infty \int_0^\infty d\tau dt_d S_{R/NR}(\tau, T, t_d) e^{\mp i\omega_\tau \tau} e^{+i\omega_{t_d} t_d} \quad (2.50)$$

ω_τ is called the absorption or excitation frequency, whilst ω_{t_d} is the emission or probe frequency. Note that the rephasing and non-rephasing spectra contain both absorptive and dispersive contributions. A pure absorptive spectrum can be produced by adding them together [5].

By obtaining spectra at different T we can observe the system’s dynamics, as illustrated in Fig. 2.9. In addition, by taking a third Fourier transform over T we can obtain the frequencies at which 2D signals oscillate and hence study the vibrations or electronic coherences which play a role in the system’s dynamics. Several papers have shown that it can be helpful to plot ‘beating maps’ from the 2D data (sometimes referred to as ‘Fourier maps’) [32–34]. These maps plot the signals which oscillate at a certain frequency during the waiting time. Specifically, instead of plotting $S_{R/NR}(\omega_\tau, T, \omega_{t_d})$, we plot [34]:

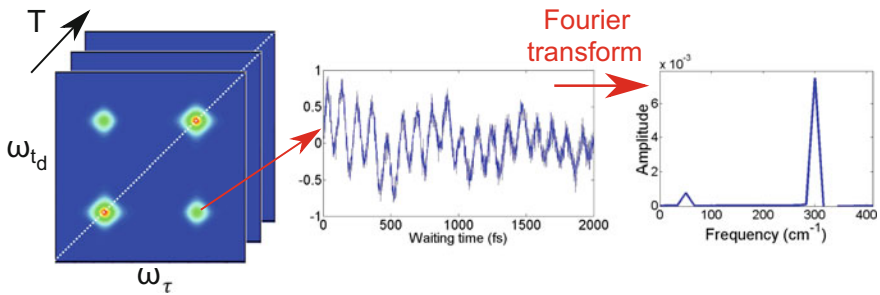


Fig. 2.9 2D spectra can be produced at different waiting times. Signals at specific points in the 2D spectrum can be plotted as a function of the waiting time and the oscillation frequencies can be obtained using a Fourier transform. Image of 2D spectrum adapted from [31]

$$A_{R/NR}(\omega_\tau, \omega_T, \omega_{t_d}) = \int_0^\infty dT \exp(i\omega_T T) \text{Re}(S_{R/NR}(\omega_\tau, T, \omega_{t_d})) \quad (2.51)$$

From the beating maps, we can learn more about the amplitude of the signals which oscillate at specific frequencies in different regions of the 2D spectrum. Notice that here the real part of the signal $S_{R/NR}(\omega_\tau, T, \omega_{t_d})$ is taken; in Chap. 3 I will discuss the additional information which can be obtained from the signal's phase.

2.3.3 Interpreting 2D Spectra

2.3.3.1 Feynman Diagrams

Expanding the commutators in the expression for the third order polarisation (Eq. 2.45) we obtain eight terms which are the response functions: R_1 , R_2 , R_3 , R_4 and their complex conjugates, for example:

$$R_3 = -\left(\frac{i}{\hbar}\right)^3 \text{Tr}(\vec{\mu}(t_d + T + \tau)\vec{\mu}(T + \tau)\rho(-\infty)\vec{\mu}(0)\vec{\mu}(\tau)) \quad (2.52)$$

The third order response functions can be visualised using Feynman diagrams [11, 25, 26]. In particular, they can be represented by four Feynman diagrams, whose structures are shown in Fig. 2.10. Time runs from the bottom to the top and the two vertical lines correspond to the ket and the bra of the density matrix. Arrows pointing towards/away from the diagram represent absorption/emission of light by the sample. Note that the final interaction, which produces the signal, must always emit light.

As an example, the term given by Eq. 2.52 is represented by the diagram labelled R_3 in Fig. 2.10. There are two interactions with the ket of the density matrix at times $T + \tau$ and $t_d + T + \tau$ and two interactions with the bra at times 0 and τ . The other terms in Eq. 2.45 correspond to the other diagrams and their complex conjugates. Note that R_2 and R_3 represent rephasing signals, whilst R_1 and R_4 correspond to non-rephasing signals. Experimentally, the rephasing and non-rephasing signals are

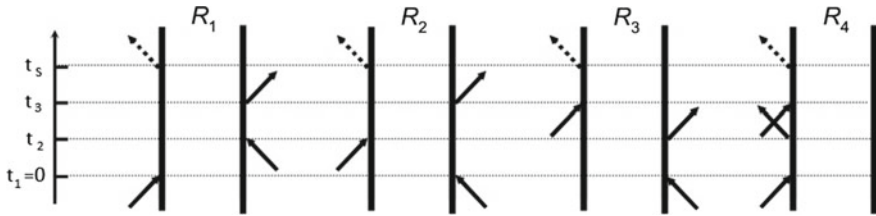


Fig. 2.10 Example Feynman diagrams [26]

observed at $\vec{k}_{I/II} = \mp \vec{k}_1 \pm \vec{k}_2 + \vec{k}_3$, as discussed previously. The rephasing signals are so-named because the signal oscillates with opposite phases during the detection and coherence times. This flip in oscillation frequency allows the system to ‘rephase’ in an analogous way to spin vectors in magnetic resonance [26].

Each Feynman diagram represents a peak in the 2D spectrum. The axes of the 2D spectrum correspond to the excitation and probe frequencies, ω_τ and ω_{td} , represented by the first and the final arrow of each Feynman diagram respectively (as discussed previously, these axes are obtained by taking a Fourier transform across the coherence and detection times). If we neglect dissipation, the amplitude of a peak in the 2D spectrum is determined by the product of the transition dipole moments involved in the Feynman diagram (illustrated by arrows in Fig. 2.10). Including dissipation will change the magnitudes of the peaks and determine their shapes in the 2D spectra. One way to approximate the effects of dissipation is to assume Markovian dephasing, in which case the lineshapes can be modelled using Lorentzian functions (we will take this approach in Chap. 3). Further discussion of the lineshapes of 2D spectra can be found for example in Cho [29].

2.3.3.2 Assigning Peaks in 2D Spectra

As discussed in Sect. 2.1, organic and biological systems are composed of a large number of interacting molecules and hence need to be described using an excitonic framework. Once the excitations of the system are known, the Feynman diagram approach described above can be applied to examine the light-induced transitions which occur between them. The system’s eigenstates form three distinct manifolds: the ground state manifold, *g*, the excited state manifold, *e*, and a higher excited manifold, *f*. Transitions between these manifolds result in three types of signals which can contribute to the peaks observed in 2D spectra: ground state bleach (GSB), stimulated emission (SE) and excited state absorption (ESA). Generic rephasing and non-rephasing Feynman diagrams for each of these signals are shown in Fig. 2.11. GSB diagrams involve dynamical evolution in the ground state manifold during the waiting time. SE and ESA diagrams evolve in the excited state manifold during the waiting time, but in SE the final transition involves emission back to the ground state manifold, whilst in ESA the final transition involves the higher excited manifold.

To illustrate how the peaks in the 2D spectra arise from the Feynman diagrams, consider an electronic dimer composed of a ground state and two excited states, *e*₁ and *e*₂, which are eigenstates of the system (see Fig. 2.12b). Two example Feynman diagrams for this system are shown in Fig. 2.13; others also exist. Diagram a leads to a diagonal peak in the 2D spectrum (i.e. one where $\omega_{td} = \omega_\tau$), since both the first and last light interactions involve a transition between *g* and *e*₁. Furthermore, the system evolves in the population state $|g\rangle\langle g|$ during the waiting time, so the corresponding peak does not oscillate as a function of the waiting time. In general, diagonal peaks are expected in the spectra at energies corresponding to exciton absorption energies.

Meanwhile, Feynman diagram b leads to an off-diagonal peak, because the initial excitation is from *g* to *e*₁, whilst the emission of light is from *e*₂ to *g*. When off-

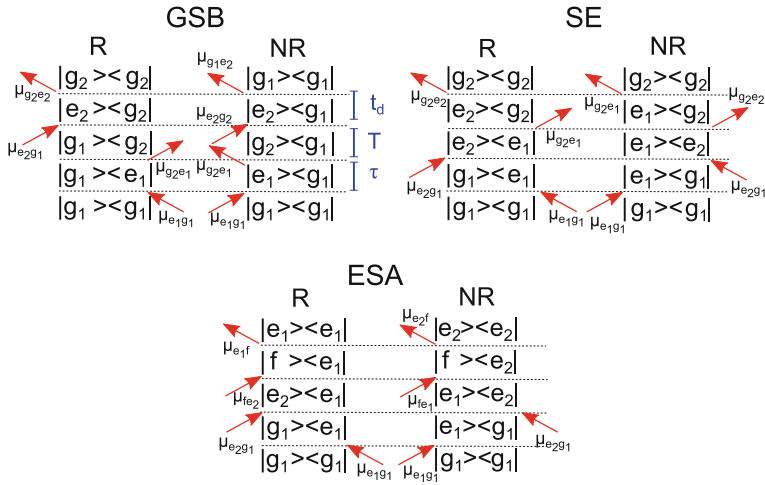


Fig. 2.11 Generic Feynman diagrams for the third-order nonlinear optical response functions [27]

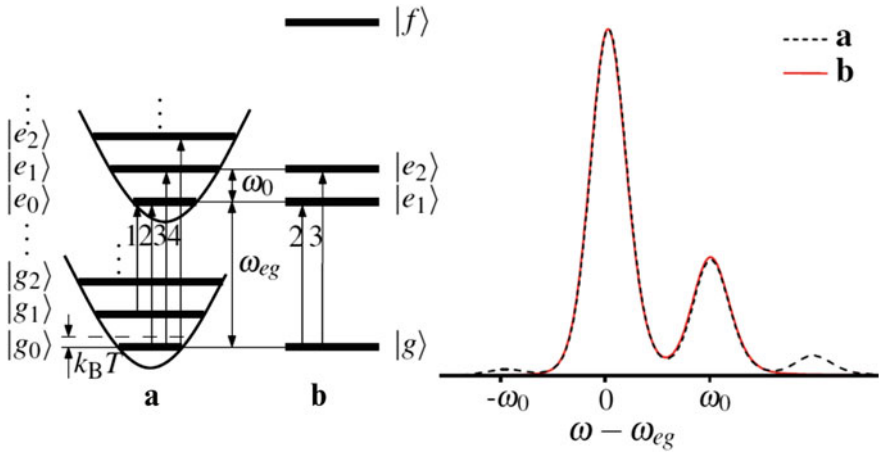
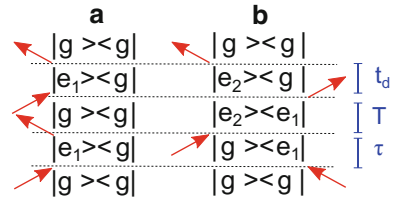


Fig. 2.12 Energy level structure of the displaced oscillator (a) and electronic dimer (b) and corresponding linear absorption spectra. Figure reprinted from [35], with permission from Elsevier

Fig. 2.13 Feynman diagrams for two peaks in the 2D spectrum of an electronic dimer system



diagonal peaks such as this one occur at short waiting times, they provide evidence for the existence of electronic couplings between pigments [5] (at longer waiting times, the picture may be complicated by energy transfer processes). Furthermore, if quantum coherences exist between the excitons, cross-peaks oscillate as a function of the waiting time with a frequency equal to the energy difference between the excitons involved [5] and this signal can be observed in the beating maps. For example, the peak from diagram b oscillates at a frequency corresponding to the energy difference between e_2 and e_1 during the waiting time and will therefore be observed in the beating map with that frequency. This is because it evolves in the quantum coherent state $|e_2\rangle\langle e_1|$ during the waiting time and the evolution of this coherent state is given by:

$$|e_1(T)\rangle\langle e_2(T)| = e^{-iE_{12}T} |e_1\rangle\langle e_2| \quad (2.53)$$

Note also that Feynman diagrams a and b in Fig. 2.13 are examples of non-rephasing and rephasing signals respectively. Measuring only the rephasing or non-rephasing signal can help to distinguish which diagrams contribute to specific peaks.

2.3.3.3 Distinguishing Electronic and Vibrational Features

Often, linear absorption spectra cannot distinguish between electronic and vibrational features. Work by Butkus et al. [35] showed that this is possible using 2DES. They considered two systems with the same linear absorption spectra: a displaced harmonic oscillator (DO) and an electronic dimer (ED), shown in Fig. 2.12. They then plotted the different peak patterns which would be expected in the 2D spectra of these two systems, see Fig. 2.14, allowing them to be distinguished. Note that here open symbols correspond to oscillatory signals, which will be observed in the corresponding frequency beating map, whilst closed symbols represent non-oscillatory signals. The differences in the patterns obtained are extremely useful to interpret complicated 2D spectra, particularly when both rephasing and non-rephasing data is available.

The electronic dimer case was discussed above; Feynman diagram a now appears as a solid (non-oscillatory) diamond at $(\omega_{eg}, \omega_{eg})$ in the non-rephasing ED diagram (Fig. 2.14, bottom right) and Feynman diagram b appears as an open (oscillatory) square at $(\omega_{eg}, \omega_{eg} + J)$ in the rephasing ED diagram (Fig. 2.14, bottom left). Note that J is related to the coupling between the sites. Notice that this means that peak b will be present in the beating maps, but not peak a. Overall, the electronic dimer non-rephasing beating map has two diagonal peaks, whilst the rephasing beating map has two off-diagonal peaks (see the open symbols in Fig. 2.14).

The displaced oscillator case can be treated similarly and gives a different set of peaks. For example, the Feynman diagram in Fig. 2.15 leads to the off-diagonal peak represented by an open diamond at $(\omega_{eg}, \omega_{eg} - \omega_0)$ in the DO rephasing diagram. This peak will oscillate due to the difference in vibrational quanta between g_0 and g_1 . Notice that unlike in the electronic dimer case, light can now be emitted at frequencies lower than ω_{eg} . This is because the final state may be the ground state

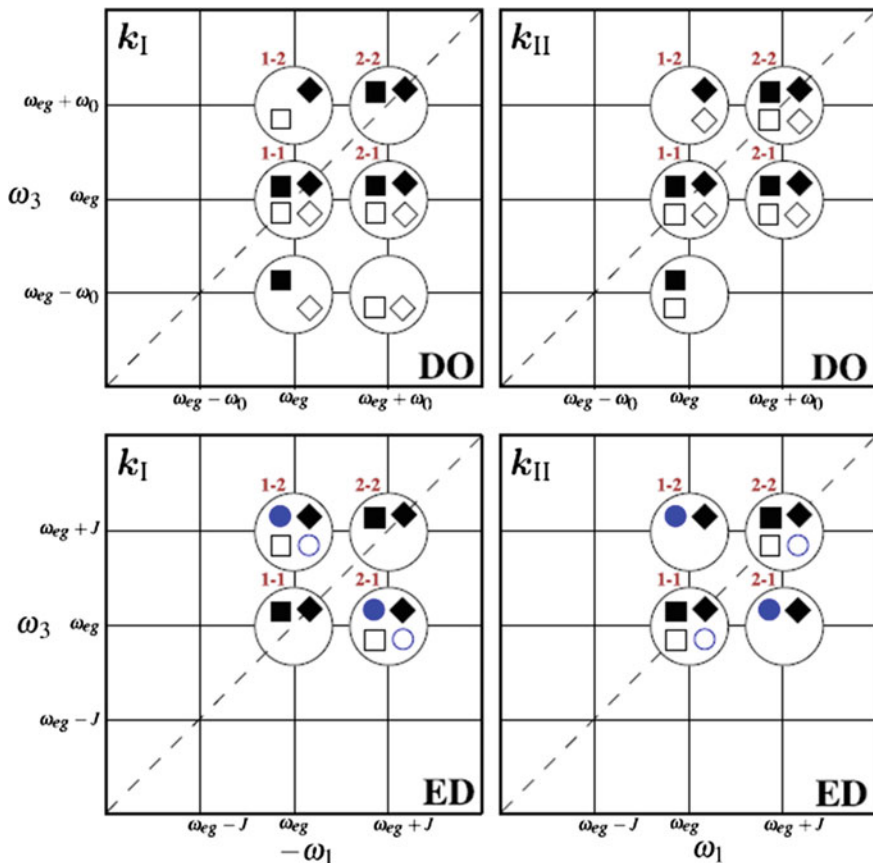
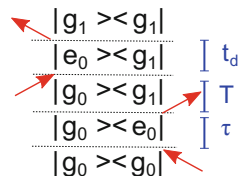


Fig. 2.14 Contributions to the 2D spectra of the rephasing (k_I) and non-rephasing (k_{II}) signals for the displaced oscillator (DO) and electronic dimer (ED) schemes. *Squares, diamonds and circles* indicate SE, GSB and ESA signals respectively. *Solid (open)* symbols denote non-oscillating (oscillating) contributions. Figure adapted from [35], with permission from Elsevier

Fig. 2.15 Feynman diagram for the peak represented by an open diamond at $(\omega_{eg}, \omega_{eg} - \omega_0)$ in the DO rephasing diagram, see Fig. 2.14



with a vibrational quantum, giving a lower probe frequency, as in Stokes scattering in Raman spectroscopy. It is normally assumed that the system is initially in the ground state with no vibrational quanta, although this assumption breaks down for low frequency modes at high temperature. There are now five peaks in each of the

rephasing and non-rephasing beating maps, compared to only two in the electronic dimer beating maps.

The characteristic electronic dimer and vibrational peak patterns described above have now been observed multiple times in the literature and provide an easy way to identify the origins of 2D signals [22, 36–38]. Nonetheless, this simplified picture should be used with care because other effects (including limited laser spectrum width) can alter the peak patterns significantly. This point will be discussed in more detail in Chap. 3.

References

1. Weiner, J., Nunes, F.: *Light-Matter Interaction: Physics and Engineering at the Nanoscale*. Oxford University Press (2013)
2. Bardeen, C.: The structure and dynamics of molecular excitons. *Annu. Rev. Phys. Chem.* **65**, 127–148 (2014)
3. van Amerongen, H., Valkunas, L., van Grondelle, R.: *Photosynthetic Excitons*. World Scientific (2000)
4. Davydov, A.: Theory of absorption spectra of molecular crystals. *Zh. Eksp. Teor. Fiz.* **18**, 210–218 (1948)
5. Schlau-Cohen, G., Ishizaki, A., Fleming, G.: Two-dimensional electronic spectroscopy and photosynthesis: Fundamentals and applications to photosynthetic light-harvesting. *Chem. Phys.* **386**, 1–22 (2011)
6. Frenkel, Y.: On the transformation of light into heat in solids I. *Phys. Rev.* **37**, 17 (1931)
7. Frenkel, Y.: On the transformation of light into heat in solids II. *Phys. Rev.* **37**, 1276 (1931)
8. Wannier, G.H.: The structure of electronic excitation levels in insulating crystals. *Phys. Rev.* **52**, 191 (1937)
9. Mott, N.F.: Conduction in polar crystals. II. The conduction band and ultra-violet absorption of alkali-halide crystals. *Trans. Farad. Soc.* **34**, 500–506 (1938)
10. Blankenship, R.: *Molecular Mechanisms of Photosynthesis*, 2 edn. Wiley-Blackwell (2014)
11. Tokmakoff, A.: *Time-Dependent Quantum Mechanics and Spectroscopy* (2016). <https://tdqms.uchicago.edu/>
12. Dexter, D.L.: A theory of sensitized luminescence in solids. *J. Chem. Phys.* **21**, 836 (1953)
13. Vos, J.G., Forster, R.J., Keyes, T.E.: *Interfacial Supramolecular Assemblies*. John Wiley and Sons, Ltd (2003)
14. Larsen, P.D.: *Dexter Energy Transfer* (2016). http://chemwiki.ucdavis.edu/Theoretical_Chemistry/Fundamentals/Dexter_Energy_Transfer
15. Weiss, U.: *Quantum Dissipative Systems*. World Scientific (2012)
16. Chin, A., Huelga, S., Plenio, M.: Chain representations of open quantum systems and their numerical simulation with time-adaptive density matrix renormalisation group methods. In: Wurfel, U., Thorwart, M., Weber, E. (eds.) *Quantum Efficiency in Complex Systems, Part II*. Academic Press (2011)
17. Blum, K.: *Density Matrix Theory and Applications*. Springer (1981)
18. Egorova, D., Kühl, A., Domcke, W.: Modeling of ultrafast electron-transfer dynamics: multi-level Redfield theory and validity of approximations. *J. Chem. Phys.* **268**, 105–120 (2001)
19. Egorova, D., Thoss, M., Domcke, W., Wang, H.: Modeling of ultrafast electron-transfer processes: validity of multilevel Redfield theory. *J. Chem. Phys.* **119**, 2761–2773 (2003)
20. Ishizaki, A., Fleming, G.R.: Unified treatment of quantum coherent and incoherent hopping dynamics in electronic energy transfer: reduced hierarchy equation approach. *J. Chem. Phys.* **130**, 234111 (2009)

21. Panitchayangkoon, G., Voronine, D.V., Abramavicius, D., Caram, J.R., Lewis, N.H.C., Mukamel, S., Engel, G.S.: Direct evidence of quantum transport in photosynthetic light-harvesting complexes. *Proc. Natl. Acad. Sci.* **108**, 20908–20912 (2011)
22. Romero, E., Augulis, R., Novoderezhkin, V.I., Ferretti, M., Thieme, J., Zigmantas, D., van Grondelle, R.: Quantum coherence in photosynthesis for efficient solar-energy conversion. *Nat. Phys.* **10**, 676–682 (2014)
23. Mohseni, M., Omar, Y., Engel, G.S., Plenio, M.B.: *Quantum Effects in Biology*. Cambridge University Press (2014)
24. Hybl, J., Albrecht, A., Faeder, S.G., Jonas, D.: Two-dimensional electronic spectroscopy. *Chem. Phys. Lett.* **297**, 307–313 (1998)
25. Mukamel, S.: *Principles of Nonlinear Optical Spectroscopy*. Oxford University Press (1995)
26. Hamm, P.: *Principles of nonlinear optical spectroscopy: a practical approach* (2005). <http://www2.chemistry.msu.edu/faculty/beck/CEM987/downloads/Hamm.pdf>
27. Bakulin, A.A., Morgan, S.E., Kehoe, T.B., Wilson, M.W.B., Chin, A.W., Zigmantas, D., Egorova, D., Rao, A.: Real-time observation of multiexcitonic states in ultrafast singlet fission using coherent 2D electronic spectroscopy. *Nat. Chem.* **8**, 16–23 (2016)
28. Fuller, F.D., Ogilvie, J.P.: Experimental implementations of two-dimensional Fourier transform electronic spectroscopy. *Annu. Rev. Phys. Chem.* **66**, 667–690 (2015)
29. Cho, M.: Coherent two-dimensional optical spectroscopy. *Chem. Rev.* **108**, 1331–1418 (2008)
30. Panman, M., Shaw, D., Ensing, B., Woutersen, S.: Local orientational order in liquids revealed by resonant vibrational energy transfer. *Phys. Rev. Lett.* **113**, 207801 (2014)
31. Huang, J.: 2D coherent spectroscopy of energy harnessing materials (2016). http://www.jyhuang.idv.tw/2DCS_maters.aspx
32. Calhoun, T.R., Ginsberg, N.S., Schlau-Cohen, G.S., Cheng, Y.-C., Ballottari, M., Bassi, R., Fleming, G.R.: Quantum coherence enabled determination of the energy landscape in light-harvesting complex II. *J. Phys. Chem. B* **113**, 16291–16295 (2009)
33. Turner, D.B., Dinshaw, R., Lee, K.-K., Belsley, M.S., Wilk, K.E., Curmick, P.M.G., Scholes, G.D.: Quantitative investigations of quantum coherence for a light-harvesting protein at conditions simulating photosynthesis. *Phys. Chem. Chem. Phys.* **14**, 4857–4874 (2012)
34. Butkus, V., Zigmantas, D., Abramavicius, D., Valkunas, L.: Distinctive character of electronic and vibrational coherences in disordered molecular aggregates. *Chem. Phys. Lett.* **587**, 93–98 (2013)
35. Butkus, V., Zigmantas, D., Valkunas, L., Abramavicius, D.: Vibrational vs. electronic coherences in 2D spectrum of molecular systems. *Chem. Phys. Lett.* **545**, 40–43 (2012)
36. Caram, J.R., Fidler, A.F., Engel, G.S.: Excited and ground state vibrational dynamics revealed by two-dimensional electronic spectroscopy. *J. Chem. Phys.* **137**, 024507 (2012)
37. Westenhoff, S., Palecek, D., Edlund, P., Smith, P., Zigmantas, D.: Coherent picosecond exciton dynamics in a photosynthetic reaction center. *J. Am. Chem. Soc.* **134**, 16484–16487 (2012)
38. Fuller, F.D., Pan, J., Gelzinis, A., Butkus, V., Senlik, S.S., Wilcox, D.E., Yocum, C.F., Valkunas, L., Abramavicius, D., Ogilvie, J.P.: Vibronic coherence in oxygenic photosynthesis. *Nat. Chem.* **6**, 706–711 (2014)

Ultrafast Quantum Effects and Vibrational Dynamics in
Organic and Biological Systems

Morgan, S.E.

2017, XV, 110 p. 72 illus., 65 illus. in color., Hardcover

ISBN: 978-3-319-63398-5